Journal of Computational Neuroscience
https://doi.org/10.1007/s10827-026-00922-z

RESEARCH

Temperature robustness of the timing network within songbird premotor nucleus HVC

Aayush Khare[1] · **Derek Sederman**[1] · **Dezhe Z. Jin**[1]

Received: 26 March 2025 / Revised: 15 January 2026 / Accepted: 16 January 2026

Abstract Many neuronal processes are temperature-sensitive. Cooling by 10 °C typically slows ion channel dynamics by more than a factor of two ($Q_{10} > 2$). Nevertheless, behaviors can remain robust despite variations in brain temperature. For instance, cooling the premotor nucleus HVC in zebra finches by 10 °C slows song production by only a factor of $Q_{10} \sim 1.3$. Here we examine the temperature robustness of the synaptic chain network within HVC. Burst spike propagation along such a chain network is postulated to control the tempo of the song. We show that the dynamics of this network are resilient to cooling and that the slowing of burst propagation exhibits a Q_{10} similar to that observed for the song. We identify two key factors underlying this robustness: the reliance on axonal delays, which are more resistant to temperature changes than ion channels, and enhanced synaptic efficacy at lower temperatures. We propose that these mechanisms represent general principles by which neural circuits maintain functional stability despite temperature fluctuations in the brain.

Significance statement Many animal behaviors remain robust despite temperature fluctuations in the brain. By studying timing circuits in songbirds, we identify key circuit elements that contribute to this resilience, including axonal delays and synaptic integration. Our work highlights how these mechanisms interact to maintain stable neuronal dynamics in response to temperature changes.

Keywords Birdsong · HVC · Temperature robustness · Timing circuits · Computational model

1 Introduction

Temperature affects most neuronal processes. Cooling decreases the activation and deactivation rates of ion channels that govern neuron dynamics (Lee et al., 2005; Schauf, 1973; Schwarz & Eikhof, 1987), slows down spike propagation along the axon (Huxley, 1959; Janssen, 1992; Moran & Melani, 2001; Swadlow et al., 1981), and reduces both synaptic and ion channel conductance (Hodgkin et al., 1952; Sterratt, 2015). In cold-blooded animals, significant fluctuations in ambient temperature can challenge the neural circuits responsible for essential behaviors (Tang et al., 2010). In contrast, warm-blooded animals, such as mammals and birds, mitigate this challenge by maintaining a constant body temperature (Tan & Knight, 2018). However, brain temperature in these animals can still fluctuate by up to 4 °C (Aronov & Fee, 2012; Kiyatkin, 2007, 2010; Moser et al., 1993), leading to detectable changes in both behavior (Aronov & Fee, 2012) and neuronal dynamics (Petersen et al., 2022). Focal cooling of specific brain areas has been used to establish causal links between brain regions and behaviors (Aronov & Fee, 2011; Aronov et al., 2011; Banerjee et al., 2021, 2019; Goldin et al., 2013; Hamaguchi et al., 2016; Long & Fee, 2008; Long et al., 2016; Petersen et al., 2022; Zhang et al., 2017).

The production of song in songbirds is controlled by the premotor nucleus HVC (proper name) and its downstream target, the robust nucleus of the arcopallium (RA) (Nottebohm et al., 1976) (Fig. 1a). Neurons in these nuclei exhibit precise spike timing that corresponds with the timing of song features. In zebra finches, HVC neurons that project to RA (HVCRA neurons) burst exactly once at precise moments during a song motif (Hahnloser et al., 2002). Furthermore, the bursts of the HVCRA neuron population form a continuous sequence that spans the entire song motif

Action Editor: Dimitris Pinotsis

✉ Dezhe Z. Jin
dzj2@psu.edu

[1] Department of Physics and Huck Institute for Life Sciences, Pennsylvania State University, University Park, PA 16802, USA

Published online: 16 February 2026

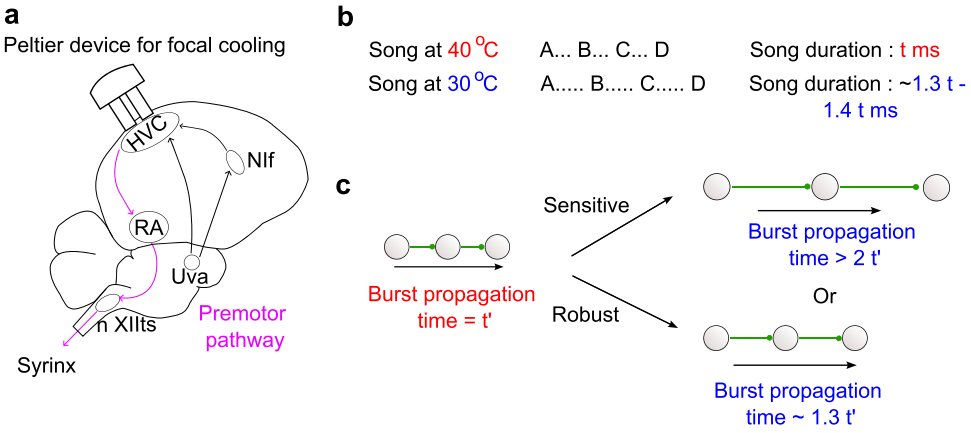

Fig. 1 Temperature robustness of song tempo. (**a**) Song production is controlled by a feedforward pathway consisting of HVC (proper name), RA (the robust nucleus of the arcopallium), and nXIIts (the tracheosyringeal nucleus of the XII cranial nerve). Additionally, a feedback pathway involves Uva (the nucleus uvaeformis) and NIf (the nucleus interface). Cooling HVC with a Peltier device slows down the song. (**b**) Cooling HVC from its normal temperature (40 °C) by 10 °C increases the song duration by a factor of 1.3 ($Q_{10}\sim$ 1.3). (**c**) In our model, song tempo is regulated by a synaptic chain network of HVCRA neurons. The central question of this study is whether this network is sensitive to or robust against temperature changes in HVC

without gaps (Egger et al., 2020; Long et al., 2010; Lynch et al., 2016; Picardo et al., 2016).

Cooling HVC by 10 °C slows the song by a factor of 1.3 (Fig. 1b). In contrast, cooling RA has minimal effect on song tempo (Long & Fee, 2008). These findings support the hypothesis that the ultra-sparse and precisely timed bursts of HVCRA neurons are generated intrinsically within the HVC via a synaptic chain network (Egger et al., 2020; Jin et al., 2007; Long et al., 2010; Tupikov & Jin, 2021). HVCRA neurons form a unidirectional synaptic chain network, where burst activity initiated at the start of the chain propagates along the network's connections (Fig. 1c). Axonal delays between HVCRA neurons, ranging from 1 to 7.5 ms, promote the formation of a polychronous network that uniformly distributes the burst times of HVCRA neurons across the song motif (Egger et al., 2020; Tupikov & Jin, 2021).

This hypothesis was challenged based on a quantitative argument regarding the effects of HVC cooling (Hamaguchi et al., 2016). The temperature sensitivity of a biological process is commonly quantified using a Q_{10} value, defined as the ratio of the rate of the process when the temperature changes by 10 °C (Huxley, 1959). A Q_{10} factor close to 1 indicates high temperature robustness. Neuronal processes, such as the activation and deactivation rates of ion channels, typically slow down with cooling, exhibiting Q_{10} values greater than 2 (Lee et al., 2005; Schauf, 1973; Schwarz & Eikhof, 1987). This raises a critical question: Why does birdsong tempo slow with a Q_{10} value of approximately 1.3 instead of $Q_{10} > 2$, as one might intuitively expect? (Hamaguchi et al., 2016) (Fig. 1c). Based on this apparent discrepancy, it was proposed that the HVC may be only one component of a distributed network involving multiple brain areas that form a loop to generate the moment-to-moment sequential activations of HVCRA neurons (Hamaguchi et al., 2016).

In this study, we use computational modeling to show that the dynamics of the synaptic chain network localized within the HVC are as robust as the song itself against HVC cooling. We identify two key mechanisms. First, spike propagation along axons is robust to temperature changes, with $Q_{10} \sim 1.25$ (Swadlow et al., 1981). Thus, the reliance on substantial axonal delays between HVCRA neurons (Egger et al., 2020; Tupikov & Jin, 2021) contributes to the temperature robustness of the synaptic chain network. Second, cooling enhances the efficacy of synaptic transmission. The decay dynamics of synaptic inputs are highly temperature-sensitive, slowing down with $Q_{10} > 2$ when cooled (Gardner, 1980; Hestrin et al., 1990). This prolongs the duration of synaptic integration (Andersen & Moser, 1995). Coupled with the rise of the resting membrane potential and a reduction in leak conductance, the extended synaptic integration broadens excitatory postsynaptic potentials (EPSPs) despite the reduction in synaptic conductance (Volgushev et al., 2000). Hence, cooling enhances synaptic efficacy between HVCRA neurons. It has been shown that excitatory inputs from the nucleus interface (NIf) elevate the membrane potentials of HVCRA neurons during singing (Otchy et al., 2015). Cooling further increases the efficacy of these inputs. These factors collectively counteract the slowing of ion channel dynamics in HVCRA neurons.

Our findings provide strong evidence that HVC is the primary site responsible for generating timing signals in birdsong. The two key factors we identify may also play a crucial role in maintaining the robustness of behaviors in

other animals, such as spatial learning in rodents, despite temperature changes in the brain (Andersen & Moser, 1995).

2 Results

The normal temperature of the zebra finch HVC is 40 °C (Aronov & Fee, 2012; Long & Fee, 2008). In this study, we investigate the changes in HVC dynamics when cooled to 30 °C.

2.1 Synaptic chain network model

In our model, the network responsible for generating precisely timed burst spikes consists of 2000 HVCRA neurons organized into a feedforward synaptic chain, similar to previous models (Egger et al., 2020; Jin et al., 2007; Long et al., 2010; Tupikov & Jin, 2021). Additionally, we include 550 HVCINT neurons to incorporate feedback inhibition into the network (Fig. 2a). Axonal delays between HVCRA neurons follow a log-normal distribution, ranging from 1.2 to 5.9 ms (5th to 95th percentile, Supplementary Fig. S1), consistent with experimental observations (Egger et al., 2020). Similarly, axonal delays from HVCRA to HVCINT neurons and from HVCINT to HVCRA neurons also follow log-normal distributions, ranging from 0.8 to 2.7 ms and 0.5 to 2.0 ms (5th to 95th percentile), respectively (Supplementary Fig. S1).

Despite distributed axonal delays, postsynaptic HVCRA neurons receive synchronous inputs, consistent with the polychronous principle (Egger et al., 2020; Izhikevich, 2006; Tupikov & Jin, 2021). A polychronous chain network can naturally emerge via a self-organizing process involving synaptic plasticity and spontaneous activity (Tupikov & Jin, 2021). In this study, we use a simplified approach to wire the polychronous chain network, which ensures nearly synchronous inputs and generates smooth burst sequences in HVCRA neurons (Methods; Supplementary Fig. S1a). This approach is far more computationally efficient than the biologically motivated self-organizing process.

Previous models of HVC networks randomly connected HVCRA and HVCINT neurons (Jin, 2009; Long et al., 2010). We find that such random wiring produces inhibitory dynamics that are inconsistent with observations of inhibition in HVC (Kosche et al., 2015). Experiments show that inhibition is gapped, such that an HVCRA neuron receives less inhibition in the time window preceding burst onset. Moreover, the membrane potentials of HVCINT neurons are intermittently elevated, with spikes riding on these elevations. In contrast, random wiring yields uniform inhibition onto HVCRA neurons, and the membrane potentials of HVCINT neurons tend to remain elevated throughout burst propagation.

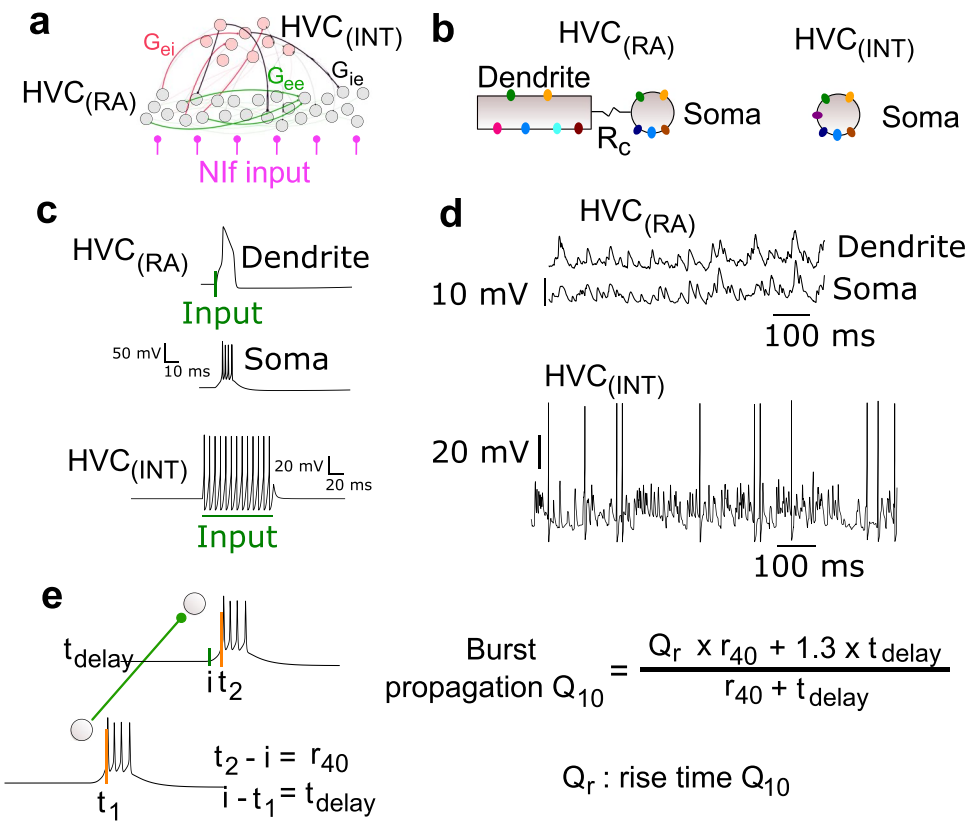

Fig. 2 The synaptic chain network model. (**a**) The HVCRA neurons form a polychronous synaptic chain network. The HVCINT neurons receive excitatory input from HVCRA neurons and provide feedback inhibition to HVCRA neurons. (**b**) The HVCRA neuron model consists of a dendritic compartment and a somatic compartment that are ohmically coupled. The HVCINT neuron is modeled as a single-compartment neuron. (**c**) Strong excitatory input to the HVCRA dendrite induces a calcium spike, which drives a stereotypical burst of action potentials in the soma. Current input to the HVCINT neuron results in high-frequency spiking activity. (**d**) Noise induces subthreshold fluctuations in both compartments of HVCRA neurons and spontaneous spike activity in HVCINT neurons. (**e**) Burst propagation between two HVCRA neurons involves two timescales: axonal delay and subthreshold integration

To mitigate these discrepancies, we introduce a structured wiring scheme between HVCRA and HVCINT neurons (Methods). Each HVCINT neuron receives inputs from 5 segments of HVCRA neurons; each segment contains on average 12 HVCRA neurons assigned consecutive burst times during construction of the polychronous chain network (Supplementary Fig. S1b). Segment start times are chosen randomly. Adjacent segments are permitted, which leads to merged segments in some cases.

To create gapped inhibition for a given HVCRA neuron, we first identify all HVCRA neurons that can provide excitatory input within a time interval preceding its burst onset (Fig. S1c), accounting for possible axonal delays. We then identify all HVCINT neurons receiving input from these HVCRA neurons and exclude them from connecting to the target HVCRA neuron. From the remaining HVCINT population, connections to the target HVCRA neuron are formed with probability $p = 0.1$ (Supplementary Fig. S1c). This gapped wiring scheme produces HVCINT dynamics that align with experimental observations (Kosche et al., 2015). Detailed comparisons between random and gapped wiring are presented in a later section.

The HVCRA neuron model consists of a dendritic compartment and a somatic compartment (Fig. 2b). Both compartments include a leak conductance. Additionally, the dendritic compartment contains calcium conductance and calcium-activated potassium conductance (Daou et al., 2013), enabling the generation of a calcium spike in response to strong input (Jin et al., 2007; Long et al., 2010). The somatic compartment contains both sodium and delayed-rectifier potassium conductances, which facilitate the generation of sodium spikes. When driven by a dendritic spike, the soma produces stereotypical bursts of 4–5 sodium spikes (Fig. 2c).

The HVCINT neuron is modeled as a single-compartment neuron (Fig. 2b) (Jin et al., 2007; Long et al., 2010). In addition to the leak, sodium, and delayed-rectifier potassium currents, it includes a high-threshold potassium current that enables spiking at high frequencies (Fig. 2c).

Noise is added to the neurons using random spike inputs to the compartments (Methods). At 40 °C, the membrane potentials of HVCRA neurons fluctuate with a standard deviation of around 3 mV (Fig. 2d); and HVCINT neurons spontaneously spike at around 10 Hz (Fig. 2d). Both values are derived from empirical observations (Hamaguchi et al., 2016; Hozhabri et al., 2025; Kozhevnikov & Fee, 2007; Long et al., 2010; Mooney, 2000; Rauske et al., 2003; Vallentin & Long, 2015).

2.2 Effects of temperature on the model parameters

The effects of temperature on neuronal processes can be categorized into three groups. The first category includes processes that depend on protein conformational changes, such as the opening and closing dynamics of ion channels and the closing dynamics of synaptic receptors. These processes are highly temperature-sensitive, with cooling significantly slowing their dynamics ($Q_{10} > 2$) (Huxley, 1959; Schauf, 1973; Schwarz & Eikhof, 1987). In our model, we set $Q_{10} = 3$ for the rates of ion channel dynamics and the decay time of synaptic conductance.

The second category includes processes involving ion diffusion driven by voltage gradients in electrolytes (Armstrong & Hille, 1998). Ion channel conductance, synaptic conductance, and the conduction of spikes in unmyelinated axons belong to this category. These processes are more temperature-robust, with Q_{10} factors of approximately 1.3 (Hodgkin et al., 1952; Sterratt, 2015). In our model, cooling reduces all conductances and increases axonal delays with $Q_{10} = 1.3$.

Finally, the reversal potentials for ion channels are directly proportional to the absolute temperature (Dayan & Abbott, 2005). Therefore, cooling from 40 °C to 30 °C results in scaling the reversal potentials by a factor of (273+30)/(273+40) = 0.97.

The scaling of all cellular parameters from 40 °C to 30 °C is summarized in Table 1.

Table 1 Changes of model parameters when temperature changed from 40 °C to 30 °C

Cellular parameter	40 °C	30 °C
Ionic Conductance	G_{ion}	$\frac{1}{1.3}\, G_{ion}$
Synaptic conductance	$g_{exc,inh}$	$\frac{1}{1.3}\, g_{exc,inh}$
Axonal delay time	t_{delay}	$1.3\, t_{delay}$
Coupling resistance (inverse of conductance)	R_c	$1.3\, R_c$
Rates	$r_{open/close}$	$\frac{1}{3.0}\, r_{open/close}$
Time constants (inverse of rates)	τ	$3\, \tau$
Reversal potential	E_{rev}	$\frac{303}{313}\, E_{rev}$

2.3 Burst propagation Q_{10}

At 40 °C, the time from the presynaptic HVCRA burst to the postsynaptic HVCRA burst consists of the axonal delay t_{delay} and the rise time r_{40} of the postsynaptic neuron's somatic membrane potential (Fig. 2e). Upon cooling to 30 °C, this burst propagation time becomes

$$\mathrm{Q_r} \times r_{40} + 1.3 \times t_{\mathrm{delay}}. \tag{1}$$

Here $\mathrm{Q_r} = r_{30}/r_{40}$, where r_{30} is the rise time of the soma's membrane potential at 30 °C. The $\mathrm{Q_{10}}$ factor for axonal delay time is 1.3 (Swadlow et al., 1981). Therefore, the $\mathrm{Q_{10}}$ factor of burst propagation time is

$$\frac{\mathrm{Q_r} \times \mathrm{r_{40}} + 1.3 \times \mathrm{t_{delay}}}{r_{40} + t_{\mathrm{delay}}}, \tag{2}$$

which is a weighted average of $\mathrm{Q_r}$ and 1.3. If $t_{\mathrm{delay}} \gg r_{40}$, the $\mathrm{Q_{10}}$ factor is closer to 1.3. Conversely, if $t_{\mathrm{delay}} \ll r_{40}$, the $\mathrm{Q_{10}}$ factor is closer to $\mathrm{Q_r}$. Experiments have shown that t_{delay} is in between 1 to 7.5 ms (Egger et al., 2020), while r_{40} is in between 5 to 10 ms (Long et al., 2010). These values indicate that axonal delay and somatic rise time contribute comparably to the burst propagation $\mathrm{Q_{10}}$ factor.

2.4 Synaptic response of an HVCRA neuron

To understand $\mathrm{Q_r}$, we examined the response of an HVCRA neuron when an excitatory synaptic input with conductance G_e was delivered to its dendrite (Fig. 3a). The rise time, r_T, was defined as the duration from the input onset to the peak of the somatic membrane potential if the response was subthreshold, or to the time of crossing -20 mV if the response was a burst of spikes (Fig. 3a). The factor $\mathrm{Q_r}$ depends on G_e, and three distinct regions can be identified (Fig. 3b).

- For $G_e < 0.29$ mS/cm^2 (region I), the neuron did not spike at either 40 °C or 30 °C. In this region, as G_e increased, $\mathrm{Q_r}$ rose from 1.73 to 3.45.
- For 0.29 mS/cm^2 $< G_e < 0.53$ mS/cm^2 (region II), the neuron did not spike at 40 °C but did spike at 30 °C. This effect arises from two factors. First, cooling reduces the leak conductance with $\mathrm{Q_{10}} = 1.3$, and the resting membrane potential is slightly elevated due to a higher leak reversal potential, making the neuron more excitable (Fig. 3c). Second, although the synaptic conductance scales down by 1.3, the synaptic decay time constant increases by a factor of $\mathrm{Q_{10}} = 3$. This results in a broadened and enhanced EPSP at 30 °C. Consequently, the membrane potential reaches higher peak values, leading to a subthreshold-to-superthreshold transition at 30 °C but not at 40 °C. This transition occurs at the left edge of region II. As G_e increases, r_{30} decreases faster than r_{40}, causing $\mathrm{Q_r}$ to decline from 3.45 to 0.48.
- For $G_e > 0.53$ mS/cm^2 (region III), the subthreshold-to-superthreshold transition also occurs at 40 °C. As G_e increases, $\mathrm{Q_r}$ rises from 0.48 and eventually plateaus at 1.42.

Example traces of somatic membrane potentials across the three regions are shown in Fig. 3c. Spike amplitudes are higher and spike widths are larger when cooled, as observed in layer 2/3 cortical neurons (Volgushev et al., 2000). The

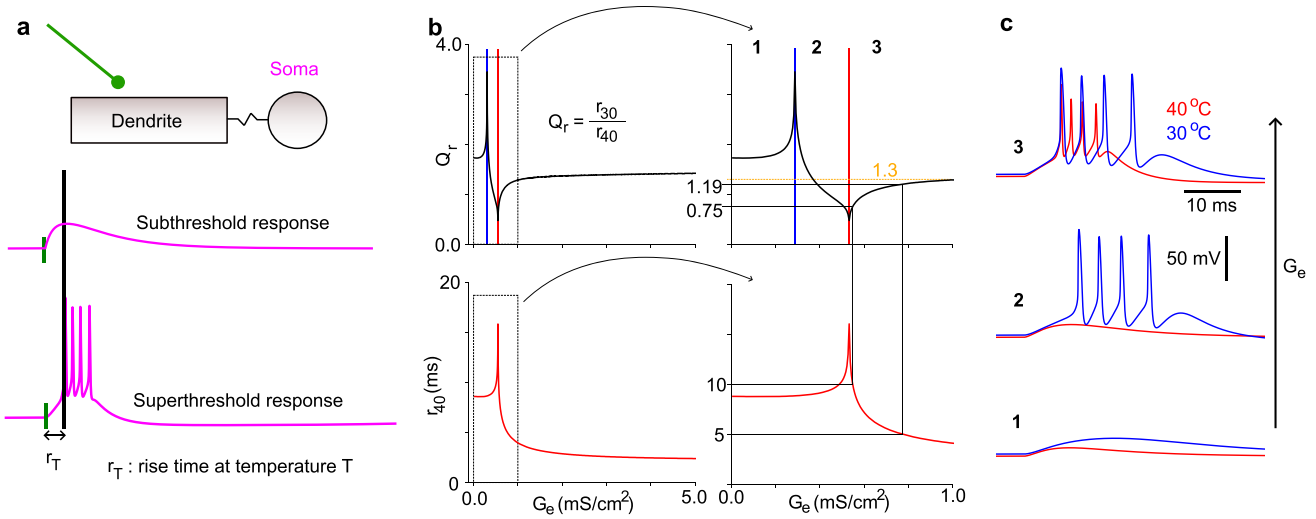

Fig. 3 The synaptic response of an HVCRA neuron. (**a**) A single excitatory synaptic input is applied at the dendrite of an HVCRA neuron, and the rise time (r_T) of the soma at a given temperature T is tracked. (**b**) The rise time r_{40} and its $\mathrm{Q_{10}}$ factor ($\mathrm{Q_r}$) as a function of the excitatory input strength G_e. Three regions are identified based on the neuronal response at two different temperatures. The right panel shows a zoomed-in section of the excitation regime, highlighting a narrow segment in region III where the rise time falls within 5–10 ms. (**c**) Example somatic membrane potential traces corresponding to the three regions identified in the analysis

Q_{10} of spike widths is around 2.1 (Fig. S2). The interspike intervals during the burst increase with cooling ($Q_{10} = 2.0$; Fig. S2).

Intracellular recordings in singing zebra finches indicate that the somatic membrane potential of HVCRA neurons rises from baseline to spiking threshold within 5 - 10 ms (Egger et al., 2020; Hamaguchi et al., 2016; Long et al., 2010). In region III of our model, increasing G_e decreases r_{40} (Fig. 3b). We find that $r_{40} = 5$ ms corresponds to $Q_r = 1.19$, while $r_{40} = 10$ ms corresponds to $Q_r = 0.75$. Thus, when r_{40} aligns with the experimental data, Q_r remains below 1.3 in our model.

These results can be understood through a simple mathematical analysis. In our model, the synaptic conductance follows a kick-and-decay dynamic (Methods). When a spike arrives, the conductance increases by G_e and then decays according to the synaptic decay time constant τ_s. The time course of the synaptic conductance is therefore given by

$$g_s(t) = G_e e^{-t/\tau_s}.$$

The subthreshold membrane potential of the dendrite can be approximated using leaky integration:

$$C_m \frac{dV}{dt} = -G_L(V - V_R) - g_s(t)V.$$

Here, C_m is the membrane capacitance, G_L is the leak conductance, and V_R is the resting membrane potential. The EPSP peaks at $t = t_m$ with $V = V_m$. At this peak,

$$\frac{dV}{dt} = 0.$$

Thus, we obtain

$$t_m = \tau_s \ln\left[\frac{G_e V_m}{G_L(V_R - V_m)}\right].$$

This equation shows that τ_s is the primary factor determining t_m. Therefore, the Q_{10} of t_m should be approximately equal to that of τ_s, which is 3 in our case. The temperature dependence of G_e and G_L cancels out. Thus, in the subthreshold regime (region I), the rise time r_T is highly sensitive to temperature.

In this subthreshold regime, cooling increases the peak value V_m of the EPSP. This occurs because the increase in τ_s, with a Q_{10} value of 3, outweighs the decrease in synaptic strength, G_e, which has a Q_{10} value of 1.3. If the membrane potential is held constant, as in a voltage-clamp experiment, the charge transfer from the synapse is proportional to

$$\int_0^\infty dt, g_s(t) = G_e \tau_s.$$

When cooled to 30 °C, this quantity increases by a factor of $3/1.3 = 2.3$. Analyzing the case where the membrane potential $V(t)$ is not clamped is more complex, but it is still possible to show mathematically that cooling increases V_m for the same reason (see Methods).

The enhanced EPSP upon cooling enables the neuron to generate dendritic calcium spikes and somatic bursts at 30 °C but not at 40 °C when G_e is further increased (region II), as shown in Fig. 3c. This dendritic spike contributes to reducing the rise time of the neuron at 30 °C, explaining why Q_r decreases in region II, as illustrated in Fig. 3b.

With sufficiently large G_e, the neuron responds with a dendritic spike and a somatic burst at 40 °C as well (region III). Notably, there remains a range of G_e where Q_r is less than 1. As G_e increases further, Q_r rises but plateaus slightly above 1.4. In this regime, a dendritic spike is rapidly generated, which in turn drives a somatic burst of spikes through the ohmic coupling R_c between the two compartments. Consequently, Q_r is largely determined by the Q_{10} of R_c and the leak conductance G_L, both of which have $Q_{10} = 1.3$. The initiation of calcium and sodium spikes is fast but has $Q_{10} = 3$, contributing to Q_r plateauing at a value slightly greater than 1.3.

2.5 Effect of NIf inputs on the HVCRA synaptic response

NIf provides major excitatory inputs to HVC (Lewandowski et al., 2013). Experiments involving the transient inactivation of NIf in zebra finches have demonstrated that NIf excitatory drive is essential for singing (Otchy et al., 2015). Interestingly, zebra finches can recover from NIf lesions, suggesting that the HVC network can homeostatically enhance connection strengths between HVCRA neurons to compensate for the loss of NIf excitatory drive (Otchy et al., 2015).

To investigate the impact of NIf excitatory drive on temperature robustness in our model, we repeated the study of the synaptic response in regime 3 (Fig. 3c) of an HVCRA neuron, now incorporating additional excitatory inputs to the dendritic compartment from NIf (Fig. 4a). The NIf input was modeled as random spikes generated by a Poisson process at 1500 Hz; at each spike, the synaptic conductance was randomly selected from $(0, G_{\mathrm{NIf}})$, where $G_{\mathrm{NIf}} = 0.005$ mS/cm^2. This value of G_{NIf} is the threshold above which the NIf input causes spontaneous activity in the HVCRA neuron. At 40 °C, this input raised the resting membrane potential from -80 mV to -76.4 mV (Fig. 4b).

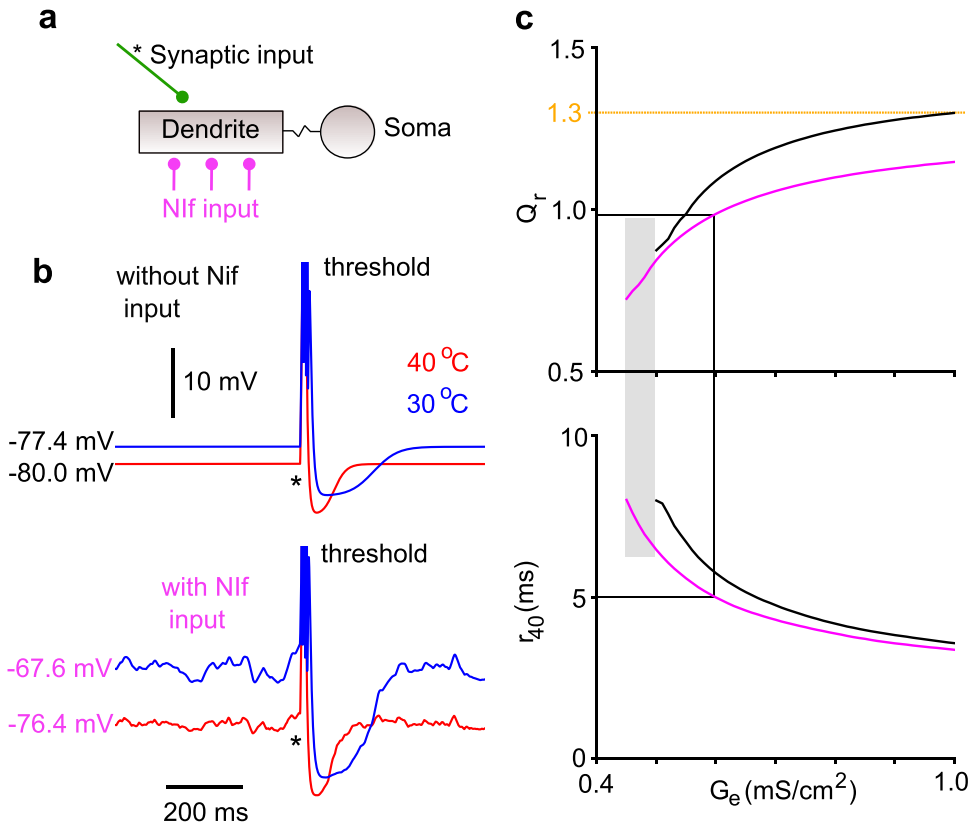

Fig. 4 The role of NIf input. (**a**) The dendrite of the HVCRA neuron receives tonic NIf input, which elevates the subthreshold membrane potential. (**b**) Membrane potential of the soma, with and without NIf input, at 40 °C and 30 °C. Cooling elevates the membrane potential more in the presence of NIf input than in its absence. Additionally, NIf input introduces membrane potential fluctuations. (**c**) With NIf input, the Q_r of the rise time is lower than without it, as observed in Q_r as a function of G_e. NIf input also facilitates burst generation at lower G_e values (shaded region). The bottom panel shows the rise time r_{40} in the presence of NIf input

Cooling reduced the NIf synaptic conductance by a factor of $Q_{10} = 1.3$, but the frequency remained unchanged because NIf activity is not affected by HVC cooling. Additionally, the synaptic decay time constant increased by $Q_{10} = 3$. Without NIf inputs, cooling to 30 °C elevated the membrane potential by 2.6 mV (Fig. 4b). In contrast, with NIf input, the membrane potential was elevated by 8.8 mV (Fig. 4b). This indicates that NIf input enhances HVCRA neuron excitability when cooled, thereby reducing the temperature sensitivity of the neuronal response. Indeed, Q_r is lower with NIf input compared to the case without it (Fig. 4c). Furthermore, NIf input enables the generation of burst responses at 40 °C even when G_e is insufficient to induce bursts in its absence (shaded region in Fig. 4c). In this regime, the r_{40} of our model HVCRA neurons was within the 5–10 ms range, and the synaptic response exhibited high temperature robustness ($Q_r < 1$).

Changing the NIf input frequency to 1000 Hz or 2000 Hz shifts the critical value of G_{NIf} above which the HVCRA neuron is spontaneously active. At these critical values for each frequency, the Q_r as a function of G_e is nearly identical to the case with a 1500 Hz frequency (Fig. S3a).

Cooling enhances the EPSPs of NIf input for the same reason described in the previous section. This enhancement further increases the temperature robustness of the synaptic responses of HVCRA neurons.

2.6 Temperature robustness of the HVC synaptic chain network

To evaluate the temperature robustness of synaptic chain network dynamics, we compared the burst propagation time at 40 °C and 30 °C (Fig. 5a). Bursts were initiated at the head of the chain network and propagated along the synaptic connections between HVCRA neurons. HVCINT neurons provided feedback inhibition to regulate the dynamics. Burst propagation time along the network was measured as the difference in the median burst times between two groups of neurons along the chain (Fig. 5a).

As expected from our analysis above, the network dynamics slowed down with cooling but remained temperature-robust. The $Q_{10,\mathrm{net}}$ of the propagation time was approximately 1.2 (Fig. 5a), similar to the Q_{10} factor by which song tempo slowed in zebra finches during HVC cooling (Long & Fee, 2008). Therefore, our network simulation demonstrates that the Q_{10} factor of song tempo observed in zebra finches is consistent with the Q_{10} factor for burst propagation along a synaptic chain network localized within HVC.

We also investigated how $Q_{10,\mathrm{net}}$ depends on the connection strength G_{ee} between HVCRA neurons and NIf inputs (Fig. 5b). Similar to the single HVCRA neuron case, increasing G_{ee} led to an increase in $Q_{10,\mathrm{net}}$. In the absence of NIf input, $Q_{10,\mathrm{net}}$ increased from 1.29 and plateaued at

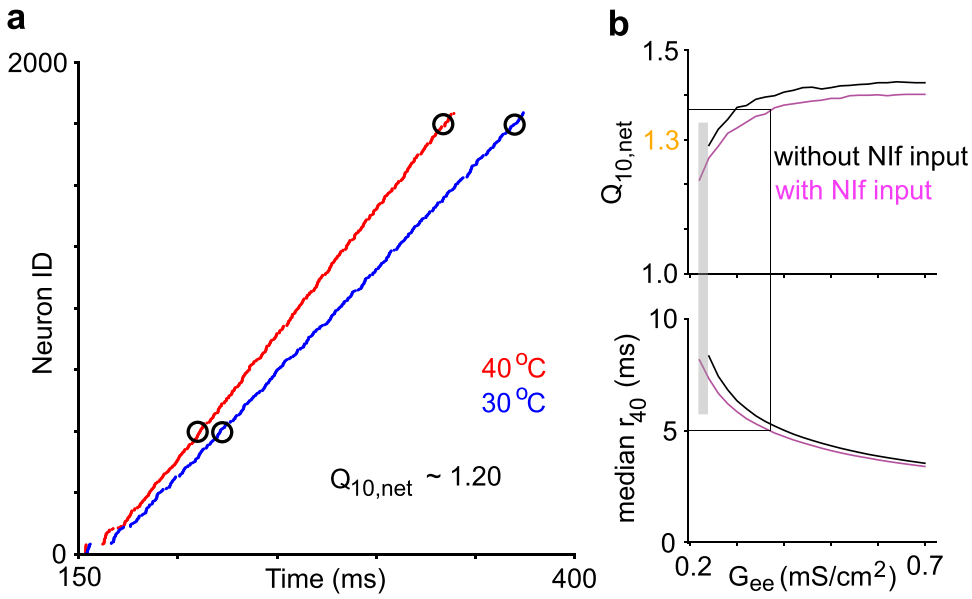

Fig. 5 Temperature robustness of burst propagation for the synaptic chain network. (**a**) Raster plot of burst onset times for HVCRA neurons at temperatures of 40 °C and 30 °C. The time required for bursts to propagate between two groups of HVCRA neurons in the network (circled) was tracked. Upon cooling, the burst propagation time increased by a factor of $Q_{10,net}$ = 1.2. (**b**) $Q_{10,net}$ as a function of the connection strength G_{ee} between HVCRA neurons. With NIf input, $Q_{10,net}$ is lower than without it. Below, the median membrane rise time r_{40} for 200 HVCRA neurons with NIf input is shown. In the shaded region, NIf input is necessary for burst propagation at 40 °C

1.43. With NIf input, $Q_{10,net}$ was lower, increasing from 1.21 and plateauing at 1.40. For values of G_{ee} for which the membrane rise time r_{40} at 40 °C was in the 5–10 ms range, $Q_{10,net}$ was in the range 1.29–1.41 without NIf input and 1.21–1.36 with NIf input. Because of feedback inhibition, G_{NIf} can be increased beyond the default value of 0.005 mS/cm^2. This lowers the minimal G_{ee} required for burst propagation, thereby extending the range of G_{ee} over which NIf input is required for burst propagation (shaded region, Fig. 5b and Fig. S3b). Varying the NIf input frequency does not alter these results (Fig. S3b).

These results also hold for a long synaptic chain network (Fig. S6), in which the number of HVCRA neurons is increased from 2000 to 10000 and the network supports burst propagation lasting about 1s at 40 °C. Thus, the temperature robustness of synaptic chain networks is not coupled to the durations of burst propagation.

2.7 Comparison of random and gapped inhibition

The gapped wiring of HVCINT neurons is important for the temperature robustness of HVC dynamics. We demonstrate this by comparing $Q_{10,net}$ with random versus gapped HVCINT wiring (Fig. 6). Simulations are run in a regime in which NIf input is required for burst propagation. Random wiring follows the procedure used in previous models (Methods; Fig. 6a-b) (Jin, 2009; Long et al., 2010). Connection probabilities are set so that, on average, the numbers of excitatory inputs onto HVCINT neurons (Fig. 6a) and inhibitory inputs onto HVCRA neurons (Fig. 6b) match those in the gapped wiring condition.

With random wiring, an HVCRA neuron receives spikes from connected HVCINT neurons at random times, including during the rise of its membrane potential toward burst onset (gray region in Fig. 6c). The membrane potentials of HVCINT neurons remain elevated throughout burst propagation (Fig. 6d). Cooling increases HVCINT firing (Fig. 6d), yielding $f_{I,30}/f_{I,40} > 1.0$ across the tested range of inhibitory conductance G_{ie} (green curve, Figure 6e). Here, $f_{I,30}$ and $f_{I,40}$ are the firing rates of HVCINT neurons at 30°C and 40°C, respectively, computed by dividing the total number of HVCINT spikes within the burst propagation time span between the two groups of neurons shown in Fig. 5a by the product of this time span and the total number of HVCINT neurons. This elevated firing is due to the increase in the synaptic time constant, which enhances synaptic integration. $Q_{10,net}$ increases with G_{ie} (green curve, Figure 6f), surpassing 2.0 at the largest inhibition strength, beyond which burst propagation ceases. This increase in $Q_{10,net}$ arises because temperature-sensitive cellular processes play a larger role in determining burst propagation speed due to the enhanced involvement of inhibition during the rising phase of HVCRA bursts.

With gapped wiring, inhibitory spikes are largely absent during the rising phase of the HVCRA membrane potential preceding burst onset (Fig. 6c). HVCINT membrane potentials are elevated only intermittently (Fig. 6d). Cooling reduces HVCINT firing, and $f_{I,30}/f_{I,40} < 1.0$ across the tested range of G_{ie} (purple curve, Figure 6e). $Q_{10,net}$ remains near 1.3 across the tested range of G_{ie} (purple curve, Figure 6f). Thus, the experimentally observed gapped inhibition is important for maintaining the temperature robustness of burst propagation in the synaptic chain network of HVCRA neurons.

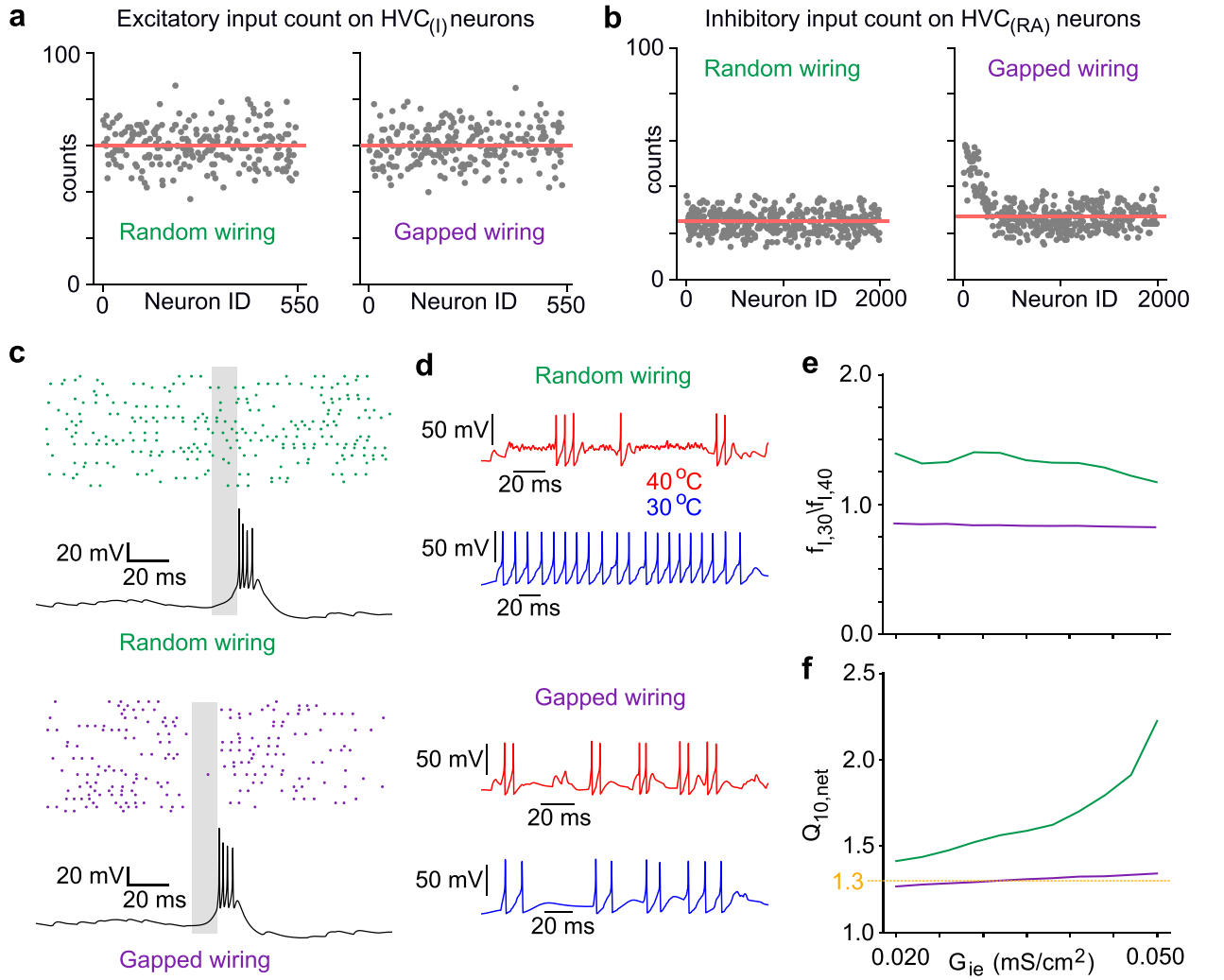

Fig. 6 Comparing random and gapped inhibition. (**a**, **b**) The networks were structured so that the numbers of connections an HVCINT neuron receives from HVCRA neurons and makes onto HVCRA neurons were similar between the random and gapped wiring configurations. (**c**) Example soma membrane potential trace of an HVCRA neuron, together with raster plots of HVCINT neurons providing inhibitory input to that HVCRA neuron. Upper: random wiring. HVCINT neurons spike in the 20 ms window before the HVCRA burst onset (gray area). Lower: gapped wiring. HVCINT neurons spike much less in this 20 ms window. (**d**) Membrane potential of an HVCINT neuron during one run at two temperatures for the random and gapped wiring configurations. (**e**) Ratios of HVCINT firing rates, f_{30}/f_{40}, for random and gapped wiring. The firing rate increases with cooling in the random wiring case (green) but decreases in the gapped wiring case (purple). (**f**) $Q_{10,\mathrm{net}}$ as a function of G_{ie} for random (green) and gapped wiring (purple)

2.8 Effects of parameter variations

We have used $Q_{10} = 3$ for ion channel and synaptic dynamics so far. To assess the impact of this choice, we also examine the network dynamics with $Q_{10} = 2$, which is often used in modeling temperature effects (Hamaguchi et al., 2016). We find that the network dynamics becomes even more robust against cooling, with $Q_{10,\mathrm{net}}$ remaining close to 1.3 across the entire range of G_{ee} tested (Fig. S4).

The distribution of axonal delays between HVCRA neurons is taken from experimental observations (Egger et al., 2020). Varying the mean and variance of this distribution by 20% produces networks with $Q_{10,\mathrm{net}}$ values that are quite similar to those obtained with the experimental distribution (Fig. S5). The distribution with a smaller mean and larger variance tends to yield a smaller $Q_{10,\mathrm{net}}$ (green curve, Figure S5c).

3 Discussion

Neuronal processes exhibit varying levels of temperature sensitivity. Cooling markedly slows ion channel dynamics (Pahlavan et al., 2023; Schwarz & Eikhof, 1987; Sterratt, 2015) and prolongs synaptic current decay ($Q_{10} > 2$) (Hestrin et al., 1990). In contrast, cooling has a moderate effect

on ion channel conductances and spike propagation speed along axons ($Q_{10} \sim 1.3$) (Hodgkin et al., 1952; Swadlow et al., 1981). Cooling the HVC region in songbirds moderately slows song speed ($Q_{10} \sim 1.3$) (Aronov & Fee, 2012; Long et al., 2010; Zhang et al., 2017). We find that this temperature robustness of song speed is consistent with a model in which the song tempo is controlled by a synaptic chain network localized within the HVC (Egger et al., 2020; Jin et al., 2007; Long et al., 2010; Tupikov & Jin, 2021). This robustness arises from the reliance on axonal delays and the enhanced efficacy of EPSPs upon cooling.

Axonal delays between HVCRA neurons are distributed over a range of 1 to 7.5 ms, with a mean of 3.3 ms (Egger et al., 2020). The synaptic chain network in our work follows the polychronous principle, where the postsynaptic neuron receives synchronous inputs from presynaptic neurons despite the distributed axonal delays (Egger et al., 2020; Izhikevich, 2006). Burst propagation time along the chain consists of two components: axonal delays from presynaptic to postsynaptic neurons and the neuronal integration time in postsynaptic neurons (Fig. 2e). Intracellular recordings of HVCRA neurons in singing zebra finches have shown that their membrane potential rises from baseline over an interval of 5 - 10 ms before burst onset. Thus, the time spent in spike propagation along axons is comparable to the time spent in neuronal integration. This reliance on axonal delays enables the network to leverage the temperature robustness of axonal conductance. In principle, local neural circuits can mitigate the impact of temperature fluctuations by relying more on axonal delays for computation.

Ion channel and synaptic decay dynamics rely on protein conformation changes and hence are highly temperature-sensitive (Sterratt, 2015). Indeed, the rates of any chemical reactions that depend on overcoming energy barriers follow the Arrhenius equation and depend exponentially on temperature (Liang, 2022). However, it is often incorrect to conclude that neural circuit dynamics and the behaviors encoded by such circuits must also be highly sensitive to temperature changes. Examples are abundant. The circadian clocks in mammalian central and peripheral tissues are almost perfectly temperature-compensated, with $Q_{10} \sim 1$ (Reyes et al., 2008). The firing rate of grasshopper auditory receptor neurons is temperature robust, with $Q_{10} \sim 1.5$ (Roemschied et al., 2014). In the pyloric circuit of the crab stomatogastric ganglion, the fraction of time the oscillator spends in bursting remains essentially constant ($Q_{10} \sim 1$) over a wide range of temperature (Alonso & Marder, 2020). Spiking of hair cells in bullfrogs maintains sensitivity and precision to sounds over a wide range of temperature (Chen & Von Gersdorff, 2019). The wingbeat frequency of locusts changes only slightly with temperature ($Q_{10} \sim 1.15$) (Robertson & Money, 2012).

Temperature-sensitive neuronal processes can exhibit counteracting properties that promote temperature robustness at the circuit level (Schapiro & Marder, 2024). In our case, cooling slows the closing of synaptic receptors, thereby enhancing synaptic transmission. Additionally, cooling elevates the resting membrane potential of neurons and reduces leak conductance, which enhances neuronal excitability, as observed in intracellular recordings of layer 2/3 pyramidal neurons in rat visual cortical slices (Volgushev et al., 2000). These effects counteract the slowing of neural integration processes and promote the temperature robustness of circuit dynamics.

NIf has been shown to provide excitatory input to HVC during singing in zebra finches (Otchy et al., 2015). Our model demonstrates that this excitatory external input also enhances the robustness of synaptic chain dynamics against cooling. The HVC network is most temperature-robust in the regime in which burst propagation requires NIf input (Fig. 5b). Indeed, experiments have shown that singing in intact zebra finches requires NIf input, because inactivating NIf stops them from singing (Otchy et al., 2015). However, our model indicates that this regime has only a limited range of allowed connection strengths G_{ee} between HVCRA neurons. Increasing NIf input strength can expand this range (Fig. S3b), but there is a limit because excessively large NIf input leads to spontaneous activity that interrupts burst propagation in the polychronous chain network. Experiments have also shown that zebra finches can recover from NIf lesions and resume singing (Otchy et al., 2015), suggesting that G_{ee} can increase in the absence of NIf input to promote burst propagation, most likely due to activity-dependent synaptic scaling (Turrigiano, 2008). We suggest that the same mechanism may also act to keep G_{ee} within the limited range that requires NIf input for burst propagation, so that the song is most robust against temperature fluctuations. Additionally, we predict that the songs of birds that have recovered from NIf lesions should be less temperature-robust than those of intact birds.

Based on experimental observations (Kosche et al., 2015), we wired the HVCRA and HVCINT neurons such that HVCRA neurons receive reduced inhibition in the 20 ms window preceding their bursts. Such gaps in inhibition prevent feedback inhibition from interfering with burst generation in HVCRA neurons (Kosche et al., 2015). In our case, these inhibition gaps ensure that the enhancement of inhibitory synapses upon cooling does not reduce the temperature robustness of burst propagation. Indeed, if we randomly wire the HVCRA and HVCINT neurons, as done in previous models (Egger et al., 2020; Jin, 2009; Long et al., 2010), inhibition gaps do not emerge (Fig. 6c). In this scenario, we find that cooling increases the firing rate of HVCINT neurons due to the enhanced efficacy of excitatory

synapses from HVCRA neurons (Fig. 6d). Additionally, cooling enhances the efficacy of inhibitory synapses onto HVCRA neurons. Together, these effects slow synaptic integration and lead to an increase in $Q_{10,net}$ (Fig. 6f). Thus, inhibition gaps play a crucial role in promoting the temperature robustness of the synaptic chain network. Such gaps can naturally arise through the self-organized wiring of the synaptic chain network via the recruitment of newborn neurons that rely on their spontaneous activity (Tupikov & Jin, 2021).

Experimentally, the membrane potentials of HVCINT neurons show intermittent elevations during singing, with spikes riding on top (Kosche et al., 2015). This contrasts with the elevated HVCINT membrane potentials throughout burst propagation at 40 °C observed in our networks with random wiring from HVCRA to HVCINT neurons (Fig. 6d). To mitigate this discrepancy, we used a wiring process that allowed an HVCINT neuron to receive inputs from a few groups of HVCRA neurons with similar burst timings. This scheme led to HVCINT membrane dynamics close to the experimental observations (Kosche et al., 2015). With this more structured wiring, cooling slightly reduces the firing rates of HVCINT neurons, in contrast to the increase seen with random wiring (Fig. 6e). It remains to be seen whether cooling reduces the firing rates of HVCINT neurons.

Inhibition in HVC has been proposed to play an important role in models of generating variable syllable sequences in the songs of species such as the Bengalese finch (Jin, 2009). During the silent gap leading to probabilistic syllable transitions, inhibition facilitates a winner-take-all mechanism for selecting the next syllable among possible candidates (Jin, 2009). Upon cooling, enhanced inhibition could slow the selection dynamics, thereby prolonging the silent gap. Indeed, experiments that cooled the Bengalese finch HVC during singing observed a larger Q_{10} for silent gaps than for syllable durations (Zhang et al., 2017), in agreement with our analysis of the role of inhibition.

A previous study questioned the synaptic chain network in HVC as the mechanism for generating sparse burst sequences in HVCRA neurons (Hamaguchi et al., 2016). The argument was that cooling HVC should result in dynamics with $Q_{10} \sim 2$, since most biological processes have $Q_{10} \sim 2$. This would contradict the observation that song Q_{10} is approximately 1.3. The authors further proposed that HVC is part of a recurrent loop network involving HVC, RA, the brainstem, and the thalamic nucleus Uvaeformis (Uva), which projects back to HVC (Hamaguchi et al., 2016). Within this framework, bursts of HVCRA neurons propagate through the loop, sequentially triggering HVCRA bursts at subsequent moments.

While this argument is plausible, it overlooks the possibility that temperature-sensitive elements within neural circuits counterbalance each other, rendering the circuit temperature-robust (Schapiro & Marder, 2024). Additionally, it does not account for the use of temperature-robust circuit elements such as axonal delays (Egger et al., 2020). Indeed, the temperature of the entire brain of a zebra finch can increase by up to 4 °C when a female is present (Aronov & Fee, 2012). The song tempo is faster, and the Q_{10} remains around 1.3, similar to the effect of cooling HVC alone (Aronov & Fee, 2012). This observation directly contradicts the intuitive expectation that $Q_{10} \sim 2$.

The recurrent loop model predicts a prominent 50 Hz oscillation in the synaptic activity of HVCRA neurons due to the time required for spikes to complete a round trip back to HVC through the loop (Hamaguchi et al., 2016). However, recordings of HVCRA neuron activity in singing zebra finches have shown no such oscillations (Egger et al., 2020).

The ion channel Q_{10} can be temperature-dependent, often decreasing at higher temperatures (Pahlavan et al., 2023). Given that birds maintain a higher average body temperature (∼40 °C) compared to mammals (∼37 °C), it is plausible that the Q_{10} for ion channels in birds may be lower than in mammals. This, in turn, would reduce $Q_{10,net}$, as shown in Fig. S4. Further experiments would be valuable in investigating this possibility.

Local axonal delays in mammalian neocortex can be widely distributed, as in HVC (Egger et al., 2020; Narayanan et al., 2015). An increase in synaptic efficacy with cooling is a general property of synapses. Thus, neural circuits in the local mammalian neocortex, like the synaptic chain in songbird HVC, can be constructed to be robust against temperature fluctuations (Andersen & Moser, 1995).

In conclusion, we have identified neuronal mechanisms that support temperature-robust burst propagation along the synaptic chain network localized within HVC. This robustness, quantified by a Q_{10} for burst propagation, is in close agreement with the observed Q_{10} ∼1.3 for the song tempo. Consequently, our findings lend further support to the role of HVC as a critical brain nucleus involved in encoding the timing and moment-to-moment features of zebra finch song.

4 Methods

4.1 HVC neuron model

The computational models of HVCRA and HVCINT neurons follow previous works (Jin, 2009; Tupikov & Jin, 2021; Wittenbach et al., 2015), and details can be found therein. We further introduced an additional ion channel in the dendritic compartment of the HVCRA neuron: the big-conductance (BK) calcium-dependent potassium channel. This channel was incorporated to ensure that calcium spikes

in the dendrite produce somatic bursts of 4 - 5 sodium spikes at both 40 °C and 30 °C. The BK channel model follows the formulation presented in Womack and Khodakhah (2002). The current is given by

$$I_{CaBK} = G_{CaBK} c_1 (E_K - V_d),$$

where $G_{CaBK} = 100$ mS/cm^2 is the channel conductance, $E_K = -90$ mV is the reversal potential of the potassium channel, and V_d is the dendritic membrane potential. The activation variable c_1 follows

$$\tau_{c_1} \frac{dc_1}{dt} = c_{1,\infty} - c_1,$$

where the time constant is $\tau_{c_1} = 2$ ms, and the steady-state value is

$$c_{1,\infty} = \frac{1}{1 + e^{(V_{1/2} - V_d)/13}}.$$

The half-activation voltage depends on the calcium concentration $[Ca]$ and is given by

$$V_{1/2} = \max(-50, 72 - 30 \log(\max(0.1, [Ca]))).$$

The calcium concentration $[Ca]$ evolves according to

$$\frac{d[Ca]}{dt} = 0.0002 I_{Ca} - \frac{[Ca]}{\tau_{Ca}},$$

where I_{Ca} is the calcium current, and $\tau_{Ca} = 50$ ms is the buffering time constant (Jin, 2009; Tupikov & Jin, 2021; Wittenbach et al., 2015).

4.2 Synaptic dynamics

We used the kick-and-decay model for synaptic dynamics, similar to previous works (Jin, 2009; Tupikov & Jin, 2021; Wittenbach et al., 2015). When a spike arrives, the synaptic conductance g increases by a fixed value G, which represents the synaptic strength. Between spikes, g decays with a synaptic time constant τ. We set $\tau = 2$ ms at 40 °C. With $Q = 3$ for τ, it increases to 6 ms at 30 °C.

4.3 Noise model

Noisy fluctuations in neuronal membrane potentials were generated by random spike inputs to the compartments (Jin, 2009). For HVCRA neurons, the dendritic and somatic compartments receive random spikes at a rate of 200 Hz, with conductance sampled uniformly from the interval (0, 0.06) mS/cm^2. For HVCINT neurons, the spike frequency was 300 Hz, with conductance sampled from the interval (0, 0.45) mS/cm^2. With equal probability, these random spikes contributed to either excitatory or inhibitory conductances of the compartment. The model HVCRA neuron's soma exhibits subthreshold fluctuations on the order of $\sim$ 3 mV (Long et al., 2010; Mooney, 2000), while the model HVCINT neuron exhibits spontaneous firing rates close to $\sim$10 Hz (Kozhevnikov & Fee, 2007).

4.4 NIf input

NIf input was modeled as random excitatory spikes generated by a Poisson process with a frequency of 1500 Hz and a conductance uniformly sampled in the range (0, 0.005) mS/cm^2. The spikes arrive at the dendritic compartment of HVCRA neurons.

4.5 Algorithm for wiring a polychronous synaptic chain network

Axonal delays of connections between HVCRA neurons are distributed in the range of 1 - 7.5 ms (Egger et al., 2020). We wired the synaptic chain network to ensure that the postsynaptic neuron receives nearly synchronous inputs from presynaptic neurons, despite the distributed axonal delays (Egger et al., 2020). We used a method that is significantly simpler than the one proposed in previous work (Egger et al., 2020).

We wired $N = 2000$ HVCRA neurons. We created 50 bins, each with a duration of 1 ms, covering a total duration of 50 ms. This represents the overall contribution of axonal delays to the burst propagation time in our network. We assigned $N_{bin} = 40$ neurons to each bin, so that the neurons in the i-th bin had putative burst onset time in the interval $t = (i, i + 1)$ ms. Each neuron sent out $N_{out} = 50$ connections. The neurons in the first bin were designated as starter neurons. These neurons were activated by external inputs to initiate burst propagation in the chain network. The neurons in the last four bins were designated as terminating neurons and do not send out connections.

We iterated over all non-terminating neurons in the order of their assigned putative burst onset times. A neuron to be wired was called a source neuron, and its putative burst onset time was denoted as t_{source}. To establish a connection, we sampled the delay time d from a log-normal distribution with a mean of 3 ms and a standard deviation of 1.5 ms. We then set the target putative burst onset time as $t_{target} = t_{source} + d$. Next, we randomly selected a neuron whose putative burst onset time fell within the range $t_{target} \pm \delta$ and established a connection from the source neuron to this target neuron with an axonal delay of d,

where $\delta = 0.25$ ms is the tolerance. This procedure was repeated until each source neuron formed all N_{out} connections. Although there was no explicit constraint on the number of input connections a neuron could receive, the number of input connections per neuron was approximately N_{out}, except for neurons in the first few bins due to the limited availability of suitable source neurons.

For each neuron, the total excitatory conductance was set to G_{ee}. The synaptic conductance of each incoming connection was then set to G_{ee}/n_{in}, where n_{in} is the number of incoming connections. This ensured that the synaptic integration time for neurons remained roughly the same, despite fluctuations in n_{in}. Additionally, the synchrony of presynaptic spike arrival was preserved, even though our wiring process did not explicitly take synaptic integration time into account.

4.6 Wiring inhibitory neurons to the synaptic chain network

Our network comprised 550 HVCINT neurons. Axonal delays were sampled from log-normal distributions with the following parameters: from HVCRA to HVCINT neurons, mean 1.55 ms and standard deviation 0.6 ms (Fig. S1h); from HVCINT to HVCRA neurons, mean 1.1 ms and standard deviation 0.5 ms (Fig. S1i). Synaptic conductances were randomly selected from the range $(0, G_{ei})$ for HVCRA -to-HVCINT connections and from the range $(0, G_{ie})$ for HVCINT -to-HVCRA connections.

Random wiring was implemented by connecting HVCINT and HVCRA neurons with fixed probabilities: 0.03 for connections from HVCRA to HVCINT and 0.045 for connections from HVCINT to HVCRA . We set the HVCRA →HVCINT synaptic conductance to $G_{ei} = 0.35$ mS/cm^2, while the HVCINT →HVCRA conductance G_{ie} was systematically varied over a range.

Gapped wiring was implemented as follows. First, each HVCINT neuron received connections from 5 segments of HVCRA neurons, each containing 12 neurons on average. HVCRA neurons within each segment were assigned consecutive putative burst times during the wiring of the polychronous chain network (Fig. S1b), so neurons within a segment tended to fire within a tight time window (< 1 ms). Segment timings were randomly selected. The separation between segments could be 0, in which case the number of segments was less than 5. We set $G_{ei} = 0.15$ mS/cm^2 to match HVCINT firing rates to those in the random wiring condition.

Second, each HVCRA neuron received connections from randomly chosen HVCINT neurons with probability $p = 0.1$, excluding all HVCINT neurons that received inputs from HVCRA neurons whose putative burst times fell within the range from $t - 7.5$ ms to $t - 1.0$ ms (Fig. S1c). Here, t denotes the putative burst onset time of the selected HVCRA neuron. HVCRA neurons with burst times in this range could deliver excitatory input during the rising phase of the selected neuron's membrane potential when axonal delays are taken into account. This exclusion thereby reduces inhibition during the rising phase of the selected HVCRA neuron.

4.7 Synaptic response of an HVCRA neuron

In the analysis of the synaptic response of an HVCRA neuron, an excitatory spike was delivered at 150 ms to the dendritic compartment, with no noise spikes present. The membrane potential rise time, r_T, at temperature T was defined as the duration from the spike input to the peak membrane potential (or the time until the membrane potential crossed -20 mV if the soma produced a burst of spikes). The input strength, G_e, was varied within the range of 0–5 mS/cm^2. The Q_{10} of the rise time was defined as $Q_r = r_{30}/r_{40}$.

4.8 Synaptic response of an HVCRA neuron with NIf input

The influence of NIf on Q_r was studied in the regime where the HVCRA neuron responded with a somatic burst of spikes at both 40 °C and 30 °C. NIf input was modeled as random excitatory spikes with a frequency of 1500 Hz using a Poisson process. The input strength of each spike was selected uniformly from the interval (0, 0.005) mS/cm^2. Noisy spikes were present. The strength of the synaptic input, G_e, varied from 0.4 to 1 mS/cm^2. The results were obtained by averaging 50 runs of the dynamics.

4.9 Calculating $Q_{10,net}$

The Q_{10} factor of burst propagation time was defined as $Q_{10,net} = \Delta t_{30}/\Delta t_{40}$, where Δt_{30} and Δt_{40} represent the differences in the median burst times of two groups of 100 HVCRA neurons at 30 °C and 40 °C, respectively. Network activity was initiated by applying a strong synaptic input of strength 1.0 mS/cm^2 to the starter neurons at $t = 150$ ms.

The dependence of $Q_{10,net}$ on the excitatory connection strength, G_{ee}, between HVCRA neurons was studied by varying G_{ee} from 0.2 to 0.7 mS/cm^2. The connection strength G_{ei}, from HVCRA to HVCINT neurons, was set to 0.15 mS/cm^2, while the connection strength G_{ie}, from HVCINT to HVCRA neurons, was set to 0.044 mS/cm^2.

The role of NIf input was studied by applying random NIf spikes to the dendritic compartment of HVCRA neurons

in the same manner as in the single-neuron case described above.

The population firing rates, $f_{I,T}$, of HVCINT neurons were computed by calculating the average spike rates of HVCINT neurons within the intervals Δt_T of the two HVCRA neuron groups.

4.10 Temperature-dependence of HVCRA burst profile

Interspike intervals (ISIs) were computed between the first two somatic spikes in each burst, defined as the time between successive crossings of a -20 mV threshold, and then averaged across bursts for each neuron and across 50 neurons. Somatic spike widths were measured at half-amplitude (the midpoint between the median baseline and the peak membrane potential) of the first spike in each burst. The median baseline was determined over the 150 ms interval preceding the synaptic input. For each neuron, first-spike widths were averaged across bursts, and these per-neuron means were then averaged across 50 neurons to calculate Q_{10} for spike width.

4.11 Analytical analysis of the leaky integration dynamics

The equation for membrane potential is

$$C_m \frac{dV}{dt} = G_L(V_R - V) - G_e e^{-t/\tau_s} V.$$

Here C_m is the membrane capacitance, G_L is the leak conductance, V_R is the resting membrane potential, G_e is the synaptic conductance, and τ_s is the synaptic decay time constant.

It is convenient to make this equation dimensionless by defining a few quantities:

$$\tau = \frac{C_m}{G_L},$$

$$g = \frac{G_e}{G_L},$$

$$\alpha = \frac{\tau}{\tau_s},$$

and

$$y = 1 - \frac{V}{V_r}.$$

Scale time as

$$t \to \frac{t}{\tau_s},$$

then the equation becomes

$$\alpha \frac{dy}{dt} = g e^{-t} - (1 + g e^{-t}) y.$$

In the $t - y$ plane, the nullcline is given by

$$\frac{dy}{dt} = 0,$$

or

$$y = \frac{g}{g + e^t}.$$

This is where the membrane potential turns around. On the left of the nullcline, $y(t)$ increases with time. On the right of the nullcline, $y(t)$ decreases with time. The nullcline is a monotonically decreasing function of t.

Because of the uniqueness theorem, solutions of the first order differential equations with the same initial condition cannot cross each other. At $t = 0$, we have

$$\frac{dy}{dt} = \frac{g}{\alpha}.$$

Therefore, small α results in a larger derivative. This makes the EPSP of a small α entirely above that of large α. In other words, small α means larger EPSP. Since cooling keeps g unchanged but decreases α, it results in a larger EPSP.

Supplementary Information The online version contains supplementary material available at https://doi.org/10.1007/s10827-026-00922-z.

Acknowledgements Supported by NSF Award EF-1822476 (DZJ). The funders had no role in study design, data collection and analysis, decision to publish, or preparation of the manuscript. We thank Michael Long for useful discussions and suggestions.

Author Contributions A.K., D.S. and D.Z.J did research. D.Z.J. wrote the manuscript and A.K. prepared all figures. All authors reviewed the manuscript.

Data Availability No datasets were generated or analysed during the current study.

Declarations

Conflicts of Interest The authors declare no competing financial interests.

Competing interests The authors declare no competing interests.

References

Alonso, L. M., & Marder, E. (2020). Temperature compensation in a small rhythmic circuit. *Elife, 9*, e55470.

Andersen, P., & Moser, E. I. (1995). Brain temperature and hippocampal function. *Hippocampus, 5*, 491–498.

Armstrong, C. M., & Hille, B. (1998). Voltage-gated ion channels and electrical excitability. *Neuron, 20*, 371–380.

Aronov, D., & Fee, M. S. (2011). Analyzing the dynamics of brain circuits with temperature: design and implementation of a miniature thermoelectric device. *Journal of Neuroscience Methods, 197*, 32–47.

Aronov, D., & Fee, M. S. (2012). Natural changes in brain temperature underlie variations in song tempo during a mating behavior. *PloS One, 7*, e47856.

Aronov, D., Veit, L., Goldberg, J. H., & Fee, M. S. (2011). Two distinct modes of forebrain circuit dynamics underlie temporal patterning in the vocalizations of young songbirds. *Journal of Neuroscience, 31*, 16353–16368.

Banerjee, A., Egger, R., & Long, M. A. (2021). Using focal cooling to link neural dynamics and behavior. *Neuron, 109*, 2508–2518.

Banerjee, A., Phelps, S. M., & Long, M. A. (2019). Singing mice. *Current Biology, 29*, R190–R191.

Chen, M., & Von Gersdorff, H. (2019). How to build a fast and highly sensitive sound detector that remains robust to temperature shifts. *Journal of Neuroscience, 39*, 7260–7276.

Daou, A., Ross, M. T., Johnson, F., Hyson, R. L., & Bertram, R. (2013). Electrophysiological characterization and computational models of hvc neurons in the zebra finch. *Journal of Neurophysiology, 110*, 1227–1245.

Dayan, P., & Abbott, L. F. (2005). *Theoretical neuroscience: computational and mathematical modeling of neural systems*. Cambridge: MIT press.

Egger, R., Tupikov, Y., Elmaleh, M., Katlowitz, K. A., Benezra, S. E., Picardo, M. A., Moll, F., Kornfeld, J., Jin, D. Z., & Long, M. A. (2020). Local axonal conduction shapes the spatiotemporal properties of neural sequences. *Cell, 183*, 537–548.

Gardner, D. (1980). Time integral of synaptic conductance. *The Journal of Physiology, 304*, 181–191.

Goldin, M. A., Alonso, L. M., Alliende, J. A., Goller, F., & Mindlin, G. B. (2013). Temperature induced syllable breaking unveils nonlinearly interacting timescales in birdsong motor pathway. *PLoS One, 8*, e67814.

Hahnloser, R. H., Kozhevnikov, A. A., & Fee, M. S. (2002). An ultrasparse code underlies the generation of neural sequences in a songbird. *Nature, 419*, 65.

Hamaguchi, K., Tanaka, M., & Mooney, R. (2016). A distributed recurrent network contributes to temporally precise vocalizations. *Neuron, 91*, 680–693.

Hestrin, S., Sah, P., & Nicoll, R. A. (1990). Mechanisms generating the time course of dual component excitatory synaptic currents recorded in hippocampal slices. *Neuron, 5*, 247–253.

Hodgkin, A. L., Huxley, A. F., & Katz, B. (1952). Measurement of current-voltage relations in the membrane of the giant axon of loligo. *The Journal of Physiology, 116*, 424.

Hozhabri, E., Asensio, A. C., Elmaleh, M., Kim, J. W., Phillips, M. B., Frazel, P. W., Dimidschstein, J., Fishell, G., & Long, M. A. (2025). Differential behavioral engagement of inhibitory interneuron subtypes in the zebra finch brain. *Neuron, 113*(3), 460–470.

Huxley, A. F. (1959). Ion movements during nerve activity. *Annals of the New York Academy of Sciences, 81*, 221–246.

Izhikevich, E. M. (2006). Polychronization: computation with spikes. *Neural Computation, 18*, 245–282.

Janssen, R. (1992). Thermal influences on nervous system function. *Neuroscience & Biobehavioral Reviews, 16*, 399–413.

Jin, D. Z. (2009). Generating variable birdsong syllable sequences with branching chain networks in avian premotor nucleus hvc. *Physical Review E, 80*, 051902.

Jin, D. Z., Ramazanoğlu, F. M., & Seung, H. S. (2007). Intrinsic bursting enhances the robustness of a neural network model of sequence generation by avian brain area hvc. *Journal of Computational Neuroscience, 23*, 283–299.

Kiyatkin, E. A. (2007). Brain temperature fluctuations during physiological and pathological conditions. *European Journal of Applied Physiology, 101*, 3–17.

Kiyatkin, E. A. (2010). Brain temperature homeostasis: physiological fluctuations and pathological shifts. *Frontiers in Bioscience: A Journal and Virtual Library, 15*, 73.

Kosche, G., Vallentin, D., & Long, M. A. (2015). Interplay of inhibition and excitation shapes a premotor neural sequence. *Journal of Neuroscience, 35*, 1217–1227.

Kozhevnikov, A., & Fee, M. S. (2007). Singing-related activity of identified HVC neurons in the zebra finch. *Journal of Neurophysiology, 97*(6), 4271–4283.

Lee, J., Callaway, J. C., & Foehring, R. C. (2005). Effects of temperature on calcium transients and ca2+-dependent afterhyperpolarizations in neocortical pyramidal neurons. *Journal of Neurophysiology, 93*, 2012–2020.

Lewandowski, B., Vyssotski, A., Hahnloser, R. H., & Schmidt, M. (2013). At the interface of the auditory and vocal motor systems: Nif and its role in vocal processing, production and learning. *Journal of Physiology-Paris, 107*, 178–192.

Liang, L. L. (2022). Temperature dependence of biological processes: Theory and applications In: *Agricultural Biocatalysis*, (pp. 89–132). Jenny Stanford Publishing.

Long, M. A., & Fee, M. S. (2008). Using temperature to analyse temporal dynamics in the songbird motor pathway. *Nature, 456*, 189.

Long, M. A., Jin, D. Z., & Fee, M. S. (2010). Support for a synaptic chain model of neuronal sequence generation. *Nature, 468*, 394.

Long, M. A., Katlowitz, K. A., Svirsky, M. A., Clary, R. C., Byun, T. M., Majaj, N., Oya, H., Howard, M. A., III., & Greenlee, J. D. (2016). Functional segregation of cortical regions underlying speech timing and articulation. *Neuron, 89*, 1187–1193.

Lynch, G. F., Okubo, T. S., Hanuschkin, A., Hahnloser, R. H., & Fee, M. S. (2016). Rhythmic continuous-time coding in the songbird analog of vocal motor cortex. *Neuron, 90*, 877–892.

Mooney, R. (2000). Different subthreshold mechanisms underlie song selectivity in identified hvc neurons of the zebra finch. *Journal of Neuroscience, 20*, 5420–5436.

Moran, O., & Melani, R. (2001). Temperature-dependent conduction properties in arctic fish peripheral nerves. *Polar Biology, 24*, 9–15.

Moser, E., & Mathiesen, l, Andersen, P. (1993). Association between brain temperature and dentate field potentials in exploring and swimming rats. *Science, 259*, 1324–1326.

Narayanan, R. T., Egger, R., Johnson, A. S., Mansvelder, H. D., Sakmann, B., De Kock, C. P., & Oberlaender, M. (2015). Beyond columnar organization: cell type-and target layer-specific principles of horizontal axon projection patterns in rat vibrissal cortex. *Cerebral Cortex, 25*, 4450–4468.

Nottebohm, F., Stokes, T. M., & Leonard, C. M. (1976). Central control of song in the canary, serinus canarius. *Journal of Comparative Neurology, 165*, 457–486.

Otchy, T. M., Wolff, S. B., Rhee, J. Y., Pehlevan, C., Kawai, R., Kempf, A., Gobes, S. M., & Ölveczky, B. P. (2015). Acute off-target effects of neural circuit manipulations. *Nature, 528*, 358–363.

Pahlavan, B., Buitrago, N., & Santamaria, F. (2023). Macromolecular rate theory explains the temperature dependence of membrane conductance kinetics. *Biophysical Journal, 122*, 522–532.

Petersen, P. C., Vöröslakos, M., & Buzsáki, G. (2022). *Brain temperature affects quantitative features of hippocampal sharp wave ripples.*

Picardo, M. A., Merel, J., Katlowitz, K. A., Vallentin, D., Okobi, D. E., Benezra, S. E., Clary, R. C., Pnevmatikakis, E. A., Paninski, L., & Long, M. A. (2016). Population-level representation of a temporal sequence underlying song production in the zebra finch. *Neuron, 90*, 866–876.

Rauske, P. L., Shea, S. D., & Margoliash, D. (2003). State and neuronal class-dependent reconfiguration in the avian song system. *Journal of Neurophysiology, 89*, 1688–1701.

Reyes, B. A., Pendergast, J. S., & Yamazaki, S. (2008). Mammalian peripheral circadian oscillators are temperature compensated. *Journal of Biological Rhythms, 23*, 95–98.

Robertson, R. M., & Money, T. G. (2012). Temperature and neuronal circuit function: compensation, tuning and tolerance. *Current Opinion in Neurobiology, 22*, 724–734.

Roemschied, F. A., Eberhard, M. J., Schleimer, J. H., Ronacher, B., & Schreiber, S. (2014). Cell-intrinsic mechanisms of temperature compensation in a grasshopper sensory receptor neuron. *Elife, 3*, e02078.

Schapiro, K., & Marder, E. (2024). Resilience of circuits to environmental challenge. *Current Opinion in Neurobiology, 87*, 102885.

Schauf, C. (1973). Temperature dependence of the ionic current kinetics of myxicola giant axons. *The Journal of Physiology, 235*, 197–205.

Schwarz, J. R., & Eikhof, G. (1987). Na currents and action potentials in rat myelinated nerve fibres at 20 and 37 c. *Pflügers Archiv, 409*, 569–577.

Sterratt, D. C. (2015). Q10: the effect of temperature on ion channel kinetics. *Encyclopedia of Computational Neuroscience* (pp. 2551–2552). New York: Springer.

Swadlow, H. A., Waxman, S. G., & Weyand, T. G. (1981). Effects of variations in temperature on impulse conduction along nonmyelinated axons in the mammalian brain. *Experimental Neurology, 71*, 383–389.

Tan, C. L., & Knight, Z. A. (2018). Regulation of body temperature by the nervous system. *Neuron, 98*, 31–48.

Tang, L. S., Goeritz, M. L., Caplan, J. S., Taylor, A. L., Fisek, M., & Marder, E. (2010). Precise temperature compensation of phase in a rhythmic motor pattern. *PLoS Biology, 8*, e1000469.

Tupikov, Y., & Jin, D. Z. (2021). Addition of new neurons and the emergence of a local neural circuit for precise timing. *PLoS Computational Biology, 17*, e1008824.

Turrigiano, G. G. (2008). The self-tuning neuron: synaptic scaling of excitatory synapses. *Cell, 135*, 422–435.

Vallentin, D., & Long, M. A. (2015). Motor origin of precise synaptic inputs onto forebrain neurons driving a skilled behavior. *Journal of Neuroscience, 35*, 299–307.

Volgushev, M., Vidyasagar, T. R., Chistiakova, M., & Eysel, U. T. (2000). Synaptic transmission in the neocortex during reversible cooling. *Neuroscience, 98*, 9–22.

Wittenbach, J. D., Bouchard, K. E., Brainard, M. S., & Jin, D. Z. (2015). An adapting auditory-motor feedback loop can contribute to generating vocal repetition. *PLoS Computational Biology, 11*, e1004471.

Womack, M. D., & Khodakhah, K. (2002). Characterization of large conductance ca2+-activated k+ channels in cerebellar purkinje neurons. *European Journal of Neuroscience, 16*, 1214–1222.

Zhang, Y. S., Wittenbach, J. D., Jin, D. Z., & Kozhevnikov, A. A. (2017). Temperature manipulation in songbird brain implicates the premotor nucleus hvc in birdsong syntax. *Journal of Neuroscience, 37*, 2600–2611.